Carbon 205 (2023) 519–526

Contents lists available at ScienceDirect

Carbon

journal homepage: www.elsevier.com/locate/carbon

# Scaling and statistics of bottom-up synthesized armchair graphene nanoribbon transistors

Yuxuan Cosmi Lin [a,*], Zafer Mutlu [a], Gabriela Borin Barin [b], Yejin Hong [a], Juan Pablo Llinas [a], Akimitsu Narita [c], Hanuman Singh [a], Klaus Müllen [c], Pascal Ruffieux [b], Roman Fasel [b,d], Jeffrey Bokor [a,e,**]

[a] Department of Electrical Engineering and Computer Sciences, University of California, Berkeley, CA, USA
[b] Empa, Swiss Federal Laboratories for Materials Science and Technology, Dübendorf, Switzerland
[c] Max Planck Institute for Polymer Research, Mainz, Germany
[d] Department of Chemistry and Biochemistry, University of Bern, Bern, Switzerland
[e] Materials Sciences Division, Lawrence Berkeley National Laboratory, Berkeley, CA, USA

ARTICLE INFO

*Keywords:*
Graphene nanoribbon
Field-effect transistor
Nanoelectronic device
Low-dimensional materials

ABSTRACT

Bottom-up assembled nanomaterials and nanostructures allow for the studies of rich and unprecedented quantum-related and mesoscopic transport phenomena. However, it can be difficult to quantify the correlations between the geometrical or structural parameters obtained from advanced microscopy and measured electrical characteristics when they are made into macroscopic devices. Here, we propose a strategy to connect the nanomaterial morphologies and the device performance through a Monte Carlo device model and apply it to understand the scaling trends of bottom-up synthesized armchair graphene nanoribbon (GNR) transistors. A new nanofabrication process is developed for GNR transistors with channel length down to 7 nm. The impacts of the GNR spatial distributions and the device geometries on the device performance are investigated systematically through comparison of experimental data with the model. Through this study, challenges and opportunities of transistor technologies based on bottom-up synthesized GNRs are pinpointed, paving the way to the further improvement of the GNR device performance for future transistor technology nodes.

## 1. Introduction

Emerging low-dimensional semiconductors have been envisioned as promising candidates for the channel materials of ultimately scaled post-silicon transistor technologies [1–3]. Among them, graphene nanoribbons (GNRs) and their heterostructures produced by on-surface or solution-processed bottom-up synthesis approaches [4–10] are of particular interest, because of their capability of defining the electronic band structures at the limit of the atomic scale, giving rise to intriguing electronic properties, including width-tunable band gaps [11], topologically engineered edge states [12,13], quantum spin chains [14–16], and steep switching induced by quantum dot and superlattice states [17–20]. Field effect transistors (FETs) made with bottom-up synthesized armchair GNRs have been demonstrated previously [21,22]. The widths and edges are perfectly defined with atomic resolution and near-unity yield, as indicated in scanning tunneling microscopic (STM) studies [4,22]. Transport measurements and theoretical analysis have shown that up to 20 μA per GNRs of on-state current with exceptional gate-control capability can be achieved for short-channel FETs representing sub-10 nm technology nodes [23]. However, a number of challenges still remain [24], such as large Schottky barriers at the metal-GNR contacts [22], GNR-GNR bundling [25,26], short GNR lengths [22,27], and chemical instability [28,29]. In addition, although the atomic structures of GNRs are nearly perfectly defined, the lengths, orientations, and locations of GNRs are randomly distributed with the current synthesis approach (see Fig. 1a). As a result, it has been difficult to correlate the overall device performance with the microscopic features obtained from advanced materials characterization approaches. In this study, we design a methodology that builds connections between the transport measurement and the advanced microscopy results of GNR samples through a Monte Carlo device model. With this approach, we are able to understand the impacts of different geometrical, physical,

* Corresponding author.
** Corresponding author. Department of Electrical Engineering and Computer Sciences, University of California, Berkeley, CA, USA.
*E-mail addresses:* yxclin@tamu.edu (Y.C. Lin), jbokor@berkeley.edu (J. Bokor).

https://doi.org/10.1016/j.carbon.2023.01.054
Received 2 November 2022; Received in revised form 17 January 2023; Accepted 27 January 2023
Available online 30 January 2023

and process-related factors on the device performance in a quantitative manner. In particular, the dimensions of FETs (channel length and channel width) are systematically varied for different types of 9-atom--wide armchair GNR (9-AGNR) samples. A new nanofabrication process is developed for GNR FETs with channel lengths down to 7 nm. Through a combination of statistical transport measurements, STM and Monte Carlo device simulations on these samples, we find clear correlations between microscopic variables of the GNR samples, such as GNR lengths, densities and spatial distributions, and macroscopic measures of device characteristics, such as the device yield, the on-state current ($I_{ON}$), the on/off current ratio ($I_{ON}/I_{OFF}$), and the subthreshold swing (SS). By comparing the experimental and the simulation results, we find that the GNR-GNR bundling and the GNR-length-limited short contact length are the major limiting factors of the device performance. This approach helps identify the current bottlenecks and future research directions for further improving the performance of GNR transistors and sets a solid foundation for quantitative electrical characterization and device physics studies for bottom-up synthesized nanoscale materials.

## 2. Methods

### 2.1. Materials synthesis and characterization

**9-AGNR Synthesis.** 9-AGNR samples were produced in a stand-alone ultrahigh-vacuum (UHV) system dubbed the "GNR reactor" - a fully automatized system that allows reproducible and high-throughput fabrication of GNRs [26]. A Au(111)/mica substrate (Phasis, Switzerland) was cleaned by two cycles of Ar + sputtering (1 keV, for 10 min) and annealing (470 °C, for 10 min). 9-AGNRs were synthesized by thermal sublimation of 3′,6′-diiodo-1,1′:2′,1″-terphenyl (DITP) [27] followed by two sequential annealing steps at 200 °C and 400 °C to activate polymerization and cyclodehydrogenation (CDH) reactions, respectively. The three molecular coverages investigated in this work were achieved by controlling both the precursor sublimation rate with a quartz microbalance and the deposition time.

**Raman Spectroscopy Measurement.** Raman characterization of the GNRs was performed using a Horiba Jobin Yvon LabRAM ARAMIS Raman microscope using a 785 nm laser with <10 mW power and a 100 × objective lens, resulting in a laser spot size of <1 μm. No thermal effects were observed under these measurement conditions, and at least three spectra from different points were collected for each sample to verify the consistency. The measurements were taken at ambient conditions.

**Scanning Tunneling Microscopy (STM).** Topographic STM images of as-grown 9-AGNRs on Au(111)/mica samples were taken with a Scienta Omicron VT-STM operated at room temperature. Constant-current STM images were recorded. The sample bias and the set point current are indicated in the associated figure captions.

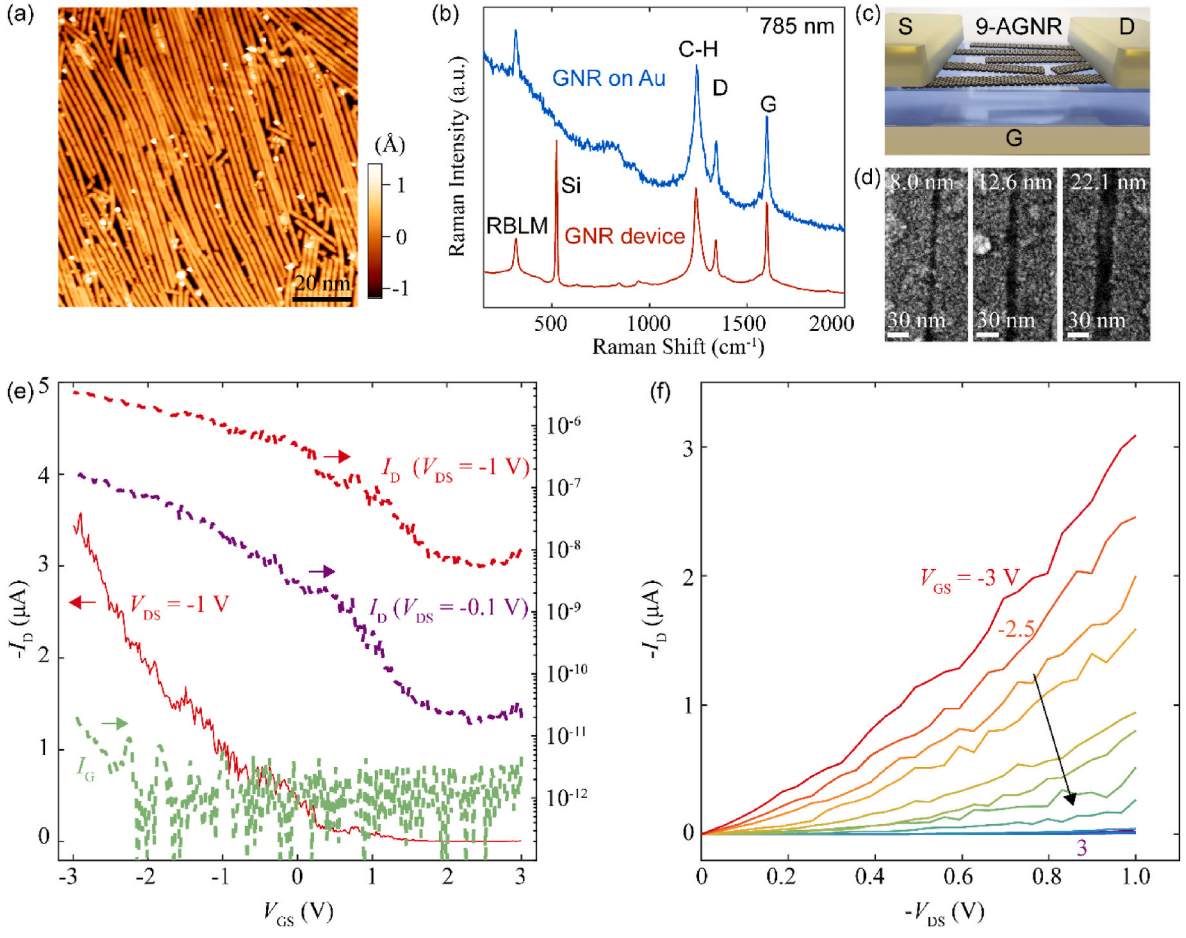


**Fig. 1.** FETs made with bottom-up synthesized 9-atom wide armchair graphene nanoribbons (9-AGNR). (a) STM image of synthesized 9-AGNR (with 1 monolayer coverage) on an Au/mica substrate with sample bias voltage ($V_s$) of −1.5 V and setpoint current ($I_t$) of 5 pA. (b) Raman spectra of 9-AGNR as synthesized on Au (blue) and after transferred onto the $HfO_2$ local bottom gate substrate. The laser excitation wavelength is 785 nm. (c) Schematic of the 9-AGNR FETs with tungsten local back gate, 5 nm $HfO_2$ gate dielectric and Pd source/drain electrodes. (d) SEM images of the as-fabricated devices with different metal gaps (channel lengths) labeled on the images. (e) $I_D - V_{GS}$ characteristic of a 9-AGNR FET in linear scale (left axis) and in logarithmic scale (right axis). The channel length ($L$) and the channel width ($W$) are 20 nm and 500 nm, respectively. (f) $I_D - V_{DS}$ characteristic of the same device with $V_{GS}$ varying from −3 V to 3 V with 0.5 V steps. (A colour version of this figure can be viewed online.)

### 2.2. Device fabrication and measurement

**Preparation of Local Bottom Gate Substrate.** The starting substrate is 100 nm $SiO_2$/Si. The local back gates are ~8 nm W deposited through sputtering, and lithographically patterned and wet etched by $H_2O_2$. The ~5.5 nm $HfO_2$ was grown in an atomic layer deposition (ALD) system (Oxford, FlexAl Plasma ALD) at 135 °C. Alignment markers and large pads for electrical probing were patterned using standard photolithography and lift-off of ~3 nm Cr and ~25 nm Pt. The wafer was then diced, and individual chips were used for further device processing.

**GNR Transfer.** First, the GNRs grown on the Au(111)/mica substrates were floated in 38% HCl in water, which caused the substrates to delaminate with the GNRs/Au film floating on the surface of the acid. Next, the floating GNRs/Au film was picked up with a local bottom gate substrate, with the GNRs facing the substrate. To increase adhesion between the gold films and substrates, a drop of isopropanol was placed onto the gold thin films (dried at ambient conditions for 5 min) followed by a hot plate baking at 100 °C for 10 min. A gold etchant solution (potassium iodine, no dilution) was used to etch the remaining gold layer. After ~5 min of etching, the samples were cleaned by soaking them in deionized water for 10 min followed by rinsing with isopropanol and dried under a stream of nitrogen.

**Patterning of Source/Drain Electrode.** After GNR transfer, the samples were spin-coated with double-layer e-beam resist (methyl methacrylate (MMA)/poly(methyl methacrylate) (PMMA)) and patterned by e-beam lithography (Crestec CABL-UH 130 kV). After development, the MMA layers were undercut, leaving suspended PMMA stripes with 100–200 nm widths as local shadow masks. Then two consecutive steps of electron-beam evaporation of 10 nm Pd with the samples tilted at the opposite angles were performed, followed by a lift-off process, leading to 10–100 nm Pd nanogaps as the channels of the FETs.

**Electrical Characterization.** The electrical characterization of the GNR FETs was performed in a Lakeshore TTPX cryogenic probe station with the vacuum level of $<10^{-5}$ torr, using an Agilent B1500 semiconductor parameter analyzer. All the measurements were performed at room temperature.

### 2.3. Device modeling

**Monte Carlo Model for GNR spatial distributions.** The length of GNRs can be represented by the gamma distribution: $l_{GNR} \sim \text{gamma}(\alpha, \beta)$, with the probability distribution function (PDF) expressed as $\text{PDF}(l_{GNR}) = \beta^{-\alpha}\Gamma^{-1}(\alpha) l_{GNR}^{\alpha-1} \exp(-l_{GNR}/\beta)$, where $\Gamma(\bullet)$ is the gamma function; $\alpha$ and $\beta$ are fitting parameters. To generate the spatial distribution of GNRs, we first determine the total number of GNRs that need to be placed on top of a given area, $N_{tot} = \rho \bullet A$, where $\rho$ is the GNR density extracted from the STM images, and $A$ is the area to be simulated. Then the lengths of the $N_{tot}$ GNRs are generated randomly according to the gamma distribution: $l_{GNR} \sim \text{gamma}(\alpha, \beta)$. Finally, each generated GNR is placed randomly onto the simulation area sequentially based on either of the following two scenarios with certain probabilities: (a) with the probability $p_a$, the current GNR is placed close to the previous one, with the center-to-center distance $\Delta c$ generated randomly from a Gaussian distribution: $\Delta c \sim \text{Gaussian}(0, \sigma_c)$, and the relative angle between the current and the previous GNRs $\Delta\theta$ also generated from a Gaussian distribution: $\Delta\theta \sim \text{Gaussian}(0, \sigma_\theta)$; (b) with the probability $p_b = 1 - p_a$, the current GNR is placed with random center position onto the simulation area. The relative angle between the current the previous GNRs $\Delta\theta$ is generated from a Gaussian distribution: $\Delta\theta \sim \text{Gaussian}(60^\circ \text{ or } 120^\circ, \sigma_\theta)$. An additional constraint needs to be met for both scenarios: the current GNR cannot overlap or be placed closer to any of the already placed GNRs than the minimum GNR-to-GNR separation, $S_{min}$. These two scenarios are chosen based on the following observations: (a) there is local alignment between neighboring GNRs with relatively small rotation angles; (b) at a larger length scale, the locally aligned GNRs form domain structures: within each domain, the GNRs are aligned, whereas in between different domains, the GNR angles are roughly 0°, 60°, and 120°, following the crystalline orientations of the Au substrates. For low-coverage (LC) samples, $\alpha = 2.47$, $\beta = 7.00$, $\rho = 0.0147\ \text{nm}^{-1}$, $\sigma_c = 2$ nm, $\sigma_\theta = 3^\circ$, $p_a = 0.999$, and $S_{min} = 2$ nm; for medium-coverage (MC) samples, $\alpha = 2.44$, $\beta = 8.05$, $\rho = 0.0273\ \text{nm}^{-1}$, $\sigma_c = 2$ nm, $\sigma_\theta = 3^\circ$, $p_a = 0.999$, and $S_{min} = 2$ nm; for high-coverage (HC) samples, $\alpha = 3.50$, $\beta = 15.23$, $\rho = 0.0188\ \text{nm}^{-1}$, $\sigma_c = 10$ nm, $\sigma_\theta = 3^\circ$, $p_a = 0.9997$, and $S_{min} = 2$ nm.

**Estimation of the On-State Current.** The total current ($I_{ON}$) can be computed by a summation of the current passing through each GNR that is connected to both source and drain ($I_n$): $I_{ON} = \sum_n I_n$. From the Monte Carlo simulation, we can find the connected GNR and its dimension parameters (length of GNR, $l_{GNR}$; the rotation angle of GNR with respect to the channel direction, $\theta$, as well as the contact length on the source and drain side, $L_S$, and $L_D$) as indicated in the red line in Fig. S1. Also, the effective channel length for this GNR is different from the channel length of the device, $L$, because of the rotation angle $\theta$, which can be expressed as $l = L/\cos(\theta)$. Assuming that the carrier scattering within the GNR channel is negligible, $I_n$ can be estimated according to the Landauer formula [30–32]:

$$I_n \propto \frac{T_S T_D}{T_S + T_D - T_S T_D} \tag{1}$$

where $T_{S(D)}$ is the transmission probability through the tunneling barrier at the source(drain) contact. Considering the finite contact length $L_{S(D)}$, $T_{S(D)}$ can be estimated by the transmission line model [33]:

$$T_{S(D)} = T_{C0} \tanh\left(\frac{L_{S(D)}}{L_T}\right) \tag{2}$$

where $T_{C0}$ is the transmission probability at the contact when the contact length is infinitely long; and $L_T$ is the transfer length, with an estimated value of 25 nm according to a previous work on carbon nanotubes [34]. Figs. S6g–i summarize the calculated $I_{ON}$ for different device dimensions and different types of 9-AGNRs based on the GNR spatial distributions obtained by the Monte Carlo simulation. In Fig. 3a and b, the simulated $I_{ON}$-$L$ curve for each type of 9-AGNRs is multiplied by a constant to roughly match the magnitudes of the experimental results.

## 3. Results and discussion

### 3.1. Field effect transistors (FETs) made with atomically precise 9-AGNRs

Fig. 1a shows a representative STM image of the as-synthesized 9-AGNRs on an Au(111)/mica substrate. The 9-AGNRs are straight and densely packed on the surface, indicating high quality of the synthesized 9-AGNRs. The 9-AGNRs are then wet-transferred [26] onto a pre-patterned local bottom-gate substrate with 5.5-nm-thick $HfO_2$ gate dielectric for further device fabrication and transport characterization (see Methods for details about synthesis, transfer, and device fabrication). To verify the fidelity of the transfer process, Raman spectroscopy measurements are performed on the samples before and after the transfer (blue and red in Fig. 1b, respectively), with an excitation laser wavelength of 785 nm. The sharp and strong peak at 314 $\text{cm}^{-1}$ corresponding to the radial breathing-like mode (RBLM) is well-preserved after transfer, suggesting that the atomic structures of the 9-AGNR samples [35,36] remain intact. After transfer, the source-drain metal contacts (Pd) are patterned by a process that involves e-beam lithographically defined local shadow masks and two steps of tilted e-beam evaporation (see Methods). With this process, it is possible to resolve channel lengths down to 7 nm. The device schematic and the top-view scanning-electron microscopic (SEM) images of the as-fabricated devices are shown in Fig. 1c, d and Fig. S2.

Fig. 1e and 1f represent typical transport characteristics of the as-fabricated 9-AGNR FET with a channel length ($L$) of 20 nm and a channel width ($W$) of 500 nm. According to the transfer characteristic (drain current, $I_D$, versus gate voltage, $V_{GS}$) as shown in Fig. 1e, p-type FET behavior is observed, with $I_{ON}$ of 3.5 μA at a drain voltage ($V_{DS}$) of 1 V, and $I_{ON}/I_{OFF}$ on the order of $10^3$, which are among the best reported values for bottom-up synthesized GNR transistors [19,21,22,37–39]. Given that the band gap of 9-AGNR has been theoretically predicted to be ~2.2 eV [11], it is in general challenging to form ohmic contact to semiconductors with such a large band gap. The super-linearity of the output characteristics ($I_D$ versus $V_{DS}$) as shown in Fig. 1f indicate the presence of a finite Schottky barrier at the metal-GNR interface, however it is considered to be more linear than previously reported results [19,21,22,37–39], indicating an improved metal contact. This improvement is likely due to the larger average GNR lengths, which will be discussed later. Devices measured in air and under vacuum exhibit similar $I_D$-$V_{GS}$ characteristics, and small hysteresis, as shown in Fig. S3.

### 3.2. Scaling and statistical trends

To investigate the impact of the length scales of GNRs on the device performance, 9-AGNR samples with various average lengths and densities are synthesized with different growth conditions, and the statistics about the length and spatial distributions are characterized with STM and captured by a Monte Carlo model. The right panels of Fig. 2a–c displays typical STM images of 9-AGNRs on Au(111)/mica substrates synthesized under LC (0.3 monolayer), MC (0.5 monolayer), and HC (1 monolayer) conditions. The GNR length ($l_{GNR}$) distributions for these three types of samples are extracted from multiple STM images as shown in Fig. 2d–f. The means and standard deviations are 17.29 nm and 11.77 nm for LC samples, 19.70 nm and 13.19 nm for MC samples, and 47.87 and 29.20 nm for HC samples. The densities of GNRs (defined as numbers of GNRs per unit area) are 0.0147 $nm^{-2}$, 0.0273 $nm^{-2}$, and 0.0188 $nm^{-2}$, respectively. It is observed that the LC and MC samples have similar GNR length distributions, while the MC and the HC samples are more densely packed than the LC sample. The asymmetric length distributions can be fitted well with the gamma distribution as shown in red solid curves in Fig. 2d–f. The spatial distributions can be further modeled by a Monte Carlo simulation with the extracted length distributions, the GNR densities and the minimum GNR-to-GNR separations as the input parameters (see Methods for details). As shown in the left panels of Fig. 2a–c, the simulated spatial distributions can capture the

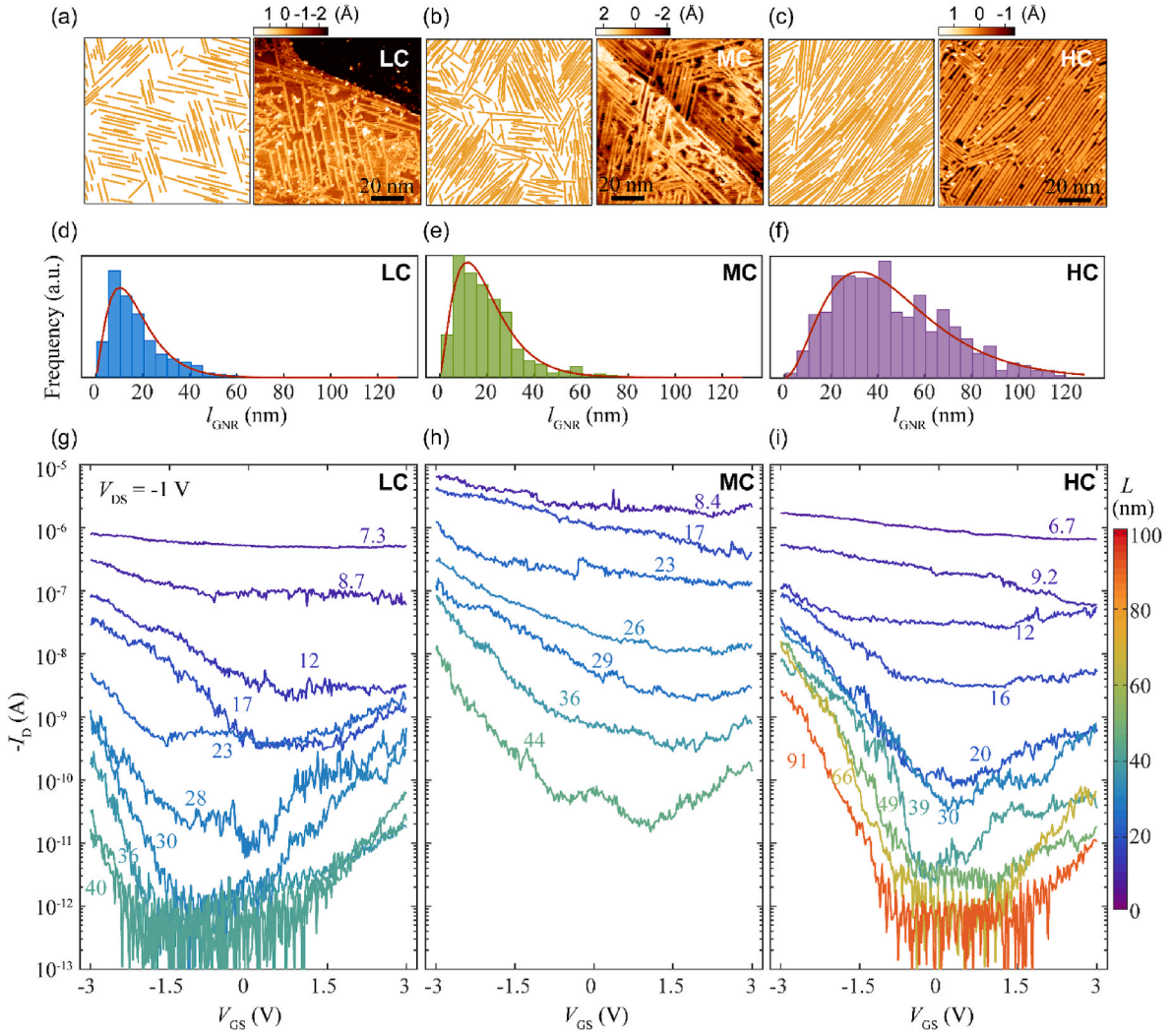


**Fig. 2.** GNR spatial distributions and channel length scaling. (a–c) Representative simulated (left) and experimentally obtained (right) STM images of LC (a), MC (b) and HC (c) 9-AGNRs on Au/mica substrates. $V_s = -1.5$ V; $I_t = 20$, 30, and 5 pA, respectively. The simulated and experimentally obtained images are on the same scale. (d–f) length distributions of LC (d), MC (e) and HC (f) 9-AGNRs extracted from multiple STM images. They are fitted with gamma distributions as shown in red curves. (g–i) Typical $I_D$-$V_{GS}$ characteristics of FETs made with LC (g), MC (h) and HC (i) 9-AGNRs with $W = 500$ nm and different $L$. The curves are color-coded and labeled with $L$ in nm. (A colour version of this figure can be viewed online.)

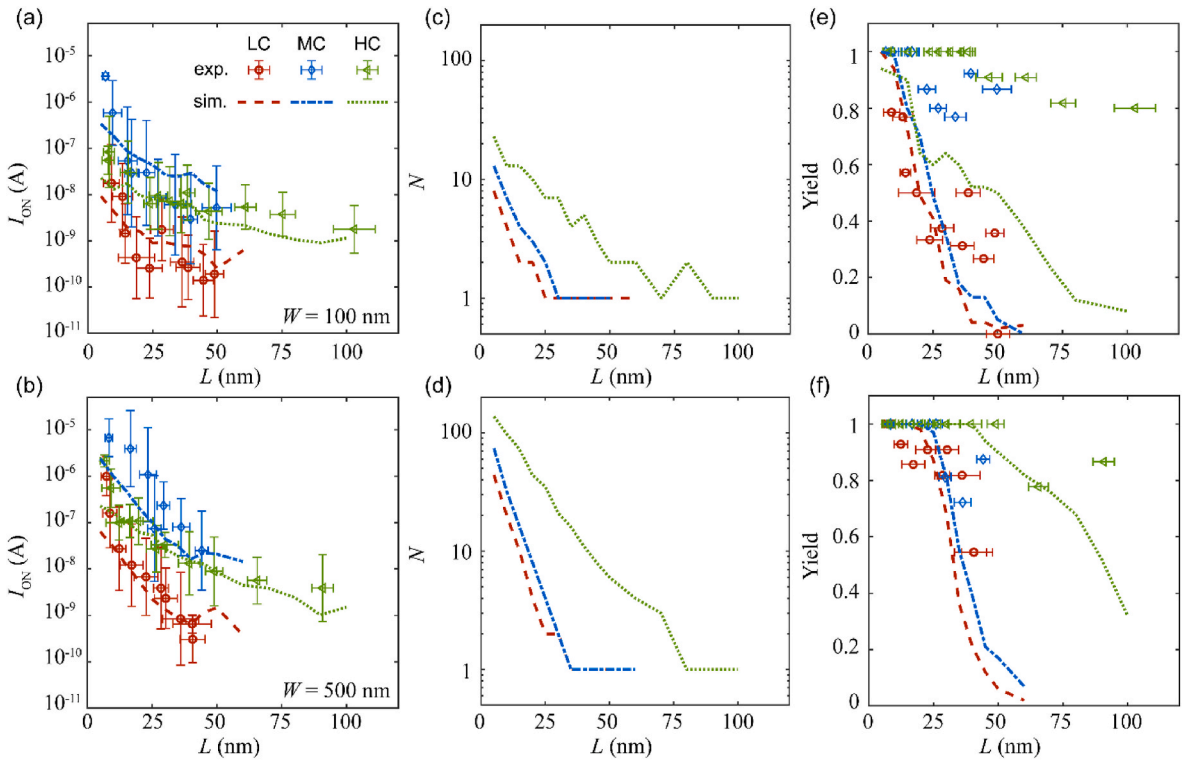


**Fig. 3.** Channel length dependence of $I_{ON}$, $N$, and device yield. (a) $I_{ON}$ versus $L$ for devices with $W = 100$ nm. (b) $I_{ON}$ versus $L$ for devices with $W = 500$ nm. (c) $N$ versus $L$ for devices with $W = 100$ nm. (d) $N$ versus $L$ for devices with $W = 500$ nm. (e) Yield versus L for devices with $W = 100$ nm. (f) Yield versus L for devices with $W = 500$ nm. The scattered points are experimental results for HC, MC and LC GNR samples. Each point is extracted from at least 10 devices with the same dimension. The dashed lines are the corresponding simulation results. (A colour version of this figure can be viewed online.)

main features observed in experimental results (STM images, right panels of Fig. 2a–c) reasonably well, especially in terms of the short-range alignment and the long-range randomness.

Raman spectroscopy measurements are taken on these three types of samples before and after transfer and device fabrication, which provides complementary valuable information about the GNRs at macroscopic scale. Figs. S4a–c displays the typical Raman spectra of the HC, MC, and LC GNRs as-grown on Au(111)/mica and the GNR devices, respectively. The presence of the well-defined characteristic RBLM, C–H mode, D, and G modes for all samples confirms the successful growth and transfer of the 9-AGNRs on Au(111)/mica [26]. When compared, the HC GNR sample has the sharpest and highest intensity RBLM peak, which indicates its high quality [26]. This result is well-consistent with the results of a recent study [40] reporting that when the molecules are more densely packed on the gold surface, the GNR quality in terms of the length and alignment is improved significantly due to the increased polymerization reaction and the reduced premature cyclodehydrogenation. The HC and MC samples are also more stable under potential processing environments [41] since the neighboring GNRs protect each other from the environmental contaminants while at the low coverage the GNR edges are more exposed to them. Moreover, while the intensities of the RBLM, G, D, and CH peaks in the Raman spectra of the HC and MC devices are almost similar, the peak intensities of the LC device are lower than those of the two devices. This result is expected since the Raman intensities are proportional to the GNR density, and it further confirms that the GNRs are seamlessly transferred.

With the help of the statistics of GNRs in the microscopic scale as discussed above, we can now better understand the statistics and scaling effects of the transport characteristics. Fig. 2g–i are representative transfer characteristics of FETs made with the three types of 9-AGNR samples, with the channel lengths ranging from 7 nm to 90 nm. To confirm that the measured $I_D$ are the current flowing through the GNR channels, instead of the gate leakage current ($I_G$), or the short-circuit current across the source-drain electrodes due to fabrication imperfections, we measured the $I_G$ as well as $I_D$ on a device with similar dimensions, but without GNRs in the channel, which are shown in Fig. S5. Both currents are several orders of magnitude smaller than the $I_D$ measured on the 9-AGNR FETs, which rules out such possibilities. Clear correlations are observed in Fig. 2g–i among the device performance, the FET channel length, and the types of 9-AGNR samples. To better capture the channel length scaling effect, we fabricate and measure tens of 9-AGNR FETs for each dimension and each GNR coverage and summarize the statistics of the key device performance metrics.

First, dramatic increases of both $I_{ON}$ and the device yield are observed as $L$ is downscaled. The scattered points in Fig. 3a and b are $I_{ON}$ versus $L$ for devices made with different types of 9-AGNR samples (plotted in different colors) and in different $W$ (100 nm and 500 nm, respectively). Please note that the change in the absolute values of $I_{ON}$ for different chips may come from batch-to-batch variations introduced during the GNR synthesis, transfer, and device fabrication processes. To account for such variations, the simulated $I_{ON}$ is normalized by an arbitrary scaling factor to better match the simulated and experimentally measured $I_{ON}$. In addition, the device yield is also improved as $L$ is reduced (Fig. 3e and f). Here, the device yield is defined as the percentage of devices, at each dimension, with their measured $I_D$ at least 10 times larger than their measured gate leakage current ($I_G$). This yield improvement is more substantial for the LC and MC samples. Both the trends for $I_{ON}$ and for device yields can be explained by the larger number of connected GNRs and the longer average contact length (defined as the overlap between the GNR and the source/drain metal contact; labeled at $L_S$ and $L_D$ in Fig. S1) of GNR-metal interfaces as the channel lengths decrease, given certain length and spatial distributions of the 9-AGNR samples. Here the contact length is still smaller or comparable to the characteristic length of the current "crowding" at the contact edge (called transfer length), which is a major limiting factor for the contact resistance of 9-AGNR FETs. This effect has also been

observed in carbon nanotubes [42].

To quantify the impacts of the device dimension and the GNR distribution on the device performance, a simplified device model is developed based on the Monte Carlo simulation results as discussed earlier. Fig. S1 illustrates a simulated GNR spatial distribution, with the box in purple dashed line indicating the active device area. Then it is straightforward to find how many GNRs are connected to both the source and the drain electrodes for each simulated device. These are the GNRs that contribute to the channel conductance. This simulation process is repeated for multiple times at each device dimension, and the resulting median numbers of connected GNRs ($N$) as a function of $L$ for different types of 9-AGNR samples are plotted in Fig. 3c, d and Figs. S6a–c. Meanwhile, the simulated device yield can be obtained if devices with $N > 0$ are considered as working devices. The simulated device yields are shown in dashed lines in Fig. 3e and f, and additional results are shown in Figs. S6d–f. An interesting observation is that the simulated and the experimental results match with each other to different extent for different samples and different device dimensions. In particular, they agree with each other very well for the LC 9-AGNR sample among various $L$ and $W$, whereas the measured yields are higher than the simulated ones for the MC and HC samples when $L$ is larger and $W$ is smaller ($W = 100$ nm in Fig. 3e). Given that the MC and HC samples have higher densities than the LC sample, we infer that the larger difference between the simulated and the experimentally extracted yields for MC and HC samples may originate from the additional inter-ribbon conductance due to GNR relocation. An underlying hypothesis for the Monte Carlo simulation is that the spatial distributions of GNRs are preserved after the device fabrication process, and as a result, no inter-ribbon electrical conductance is considered. This hypothesis may not be accurate, as relocation of GNRs may take place especially during the wet-transfer process, and the neighboring GNRs are likely to contact, or bundle with one another, leading to the inter-ribbon conductance [26]. It is noted that the GNR relocation may only cause very slight shifts of each GNRs, thus the overall GNR spatial distributions can still be approximated by the Monte Carlo model. Assuming similar degrees of GNR relocation for the three types of 9-AGNR samples, the higher density, or lower GNR-GNR spacing in MC and HS samples would give rise to a higher probability of physical contact of neighboring GNRs and more contributions from the inter-ribbon conductance. Therefore, the higher yields measured on devices with larger $L$ and smaller $W$ for these two types of samples can be attributed to the longer-range and winding conduction paths of interconnected GNRs within and outside the channel regions, respectively.

The total on-current $I_{ON}$ for each device can be computed by the summation of the current passing through each GNR that is connected to the source and drain electrodes. To estimate the single-GNR current, a simplified model is used based on the Landauer formula [30] with the considerations of the transmission probability through the source/drain contact barriers and the effect of short contact length (see Methods for details). Fig. 3a and b displays the simulated and experimental average $I_{ON}$ for the three types of 9-AGNR samples when $W = 100$ nm and 500 nm, respectively, and they are in reasonable agreement with each other. Figs. S6g–i show additional simulated $I_{ON}$ with various device dimensions. We thus conclude that the negative correlation between $I_{ON}$ and $L$ are mainly because of the change in the number of connected GNRs in the channel, as well as the change in the contact length. In addition, the slightly faster $I_{ON}$ drop with $L$ in the shorter $L$ regime ($L <$ 20 nm) observed in experiments may come from defect scattering in the channel [43], and the more gradual tail in the longer $L$ regime ($L > 50$ nm for the HC sample) may be another indication of the inter-ribbon conductance as mentioned earlier. In addition, the much lower $I_{ON}$ for the LC sample can be attributed to both the smaller number of connected GNRs and the lower GNR quality than those of HC and MC samples as substantiated by the Raman spectroscopy results as discussed earlier (Fig. S4).

Second, the gate coupling efficiency is also strongly correlated with the channel length, as suggested by the scaling trends for both the $I_{ON}/I_{OFF}$ and the SS as shown in Fig. 4a and b, respectively. Here, SS is defined as $SS = |d\lg(I_D)/dV_{GS}|^{-1}$, and the minimum SS among different $V_{GS}$ is selected to represent the performance of each device in Fig. 4b. The average $I_{OFF}$ as a function of $L$ are also shown in Fig. S7a. At the long-channel limit, the average $I_{ON}/I_{OFF}$ is as high as $10^4$, and the average SS is as low as 100 mV/dec, which indicate good gate coupling efficiencies. However, when $L$ becomes smaller, the average $I_{ON}/I_{OFF}$ decreases exponentially and the average SS increases exponentially, corresponding to a fast degradation of the gate control. The transition between the flat and the fast-changing regimes happens at the critical channel length $L_{cr} \approx 30$ nm. However, for an ideal single-GNR channel on a 5.5-nm-$HfO_2$ gate dielectric, the scaling length $\lambda$ is estimated to be only ~2 nm [44], which is much lower than $L_{cr}$. Such a discrepancy could be attributed to two factors: (1) GNR-GNR screening, in which the neighboring GNRs in a densely packed sample screen the fringe capacitance of each GNR channel, leading to a weakened gate coupling efficiency; (2) GNR relocation and bundling, in which there might be a chance that neighboring GNRs are on top of each other, resulting in a higher effective body thickness. In future work, aligned GNRs with low density [45] and dry transfer techniques can be adapted to address these issues. Furthermore, the bottom-gate device geometry can be replaced by a dual-gate or a gate-all-around geometry to further improve the gate coupling efficiency and to enable the further downscaling of GNR transistors [44,46,47].

Third, the source/drain metal contact to the GNR channel is improved for the longer GNR samples (HC 9-AGNR). As shown in Fig. 4c, the $I_D$-$V_{DS}$ curve for the MC sample is very nonlinear, indicating a large Schottky barrier tunneling resistance at the metal-semiconductor contact, whereas the $I_D$-$V_{DS}$ curve for the HC sample with the same device dimension is almost linear, indicating a better metal contact. To quantify this effect, we define the nonlinearity NL as $NL = I_D(V_{DS} = -1\ V)/[10I_D(V_{DS} = -0.1\ V)]$: larger NL (greater than 1) means stronger superlinear $I_D$-$V_{DS}$ relation; and $NL = 1$ corresponds to linear $I_D$-$V_{DS}$ relation. The average NL for the three types of 9-AGNR samples for various $L$ and $W$ are plotted in Fig. 4d. A systematically lower NL is observed on the HC 9-AGNR sample than on the LC and MC samples, for the same $L$. This trend is further substantiated by the systematically lower drain-induced barrier lowering (DIBL) for the HC sample as shown in Fig. S7b. We thus conclude that such a nonlinearity improvement for the HC sample is associated with the larger contact length, or the larger overlap between the GNR channels and the source/drain electrodes.

## 4. Conclusion

In summary, through varying the device geometry and extracting the statistical trends of the device parameters, the correlations between the GNR microscopic morphologies and the device performance of the GNR FETs are obtained. With a combined theoretical and experimental approach, the effects of the GNR spatial distributions, the GNR-GNR relocation and bundling during the device fabrication processes, and the overlaps between the metal contacts and the GNR channel are quantitatively investigated. Based on our analysis, we identify the factors limiting GNR devices fabricated using the present technologies, and anticipate that further improvement of the device performance be achieved for aligned GNR samples with longer GNR lengths and controlled GNR densities.

## Notes

The authors declare no competing financial interest.

## CRediT authorship contribution statement

**Yuxuan Cosmi Lin:** Formal analysis, Conceptualization, Data curation, Investigation, Methodology, Writing – original draft, Writing –

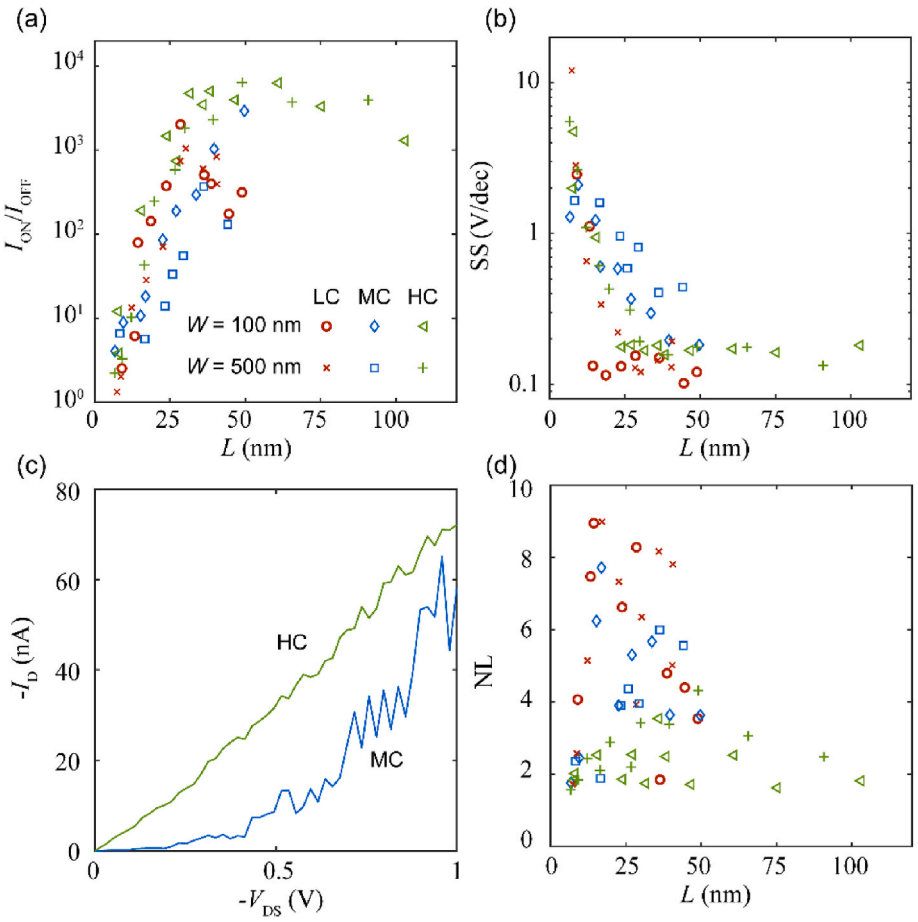


**Fig. 4.** Channel length dependence of $I_{ON}/I_{OFF}$, SS, and NL. (a) Average $I_{ON}/I_{OFF}$ versus $L$ at $V_{DS} = -1$ V. (b) Average SS versus $L$ at $V_{DS} = -0.1$ V. (c) $I_D - V_{DS}$ curves of typical MC and HC devices with $L = 23$ nm, $W = 500$ nm, at $V_{GS} = -3$ V. (d) Average NL versus $L$ at $V_{GS} = -3$ V. (A colour version of this figure can be viewed online.)

review & editing. **Zafer Mutlu:** Formal analysis, Conceptualization, Data curation, Investigation, Methodology, Writing – review & editing. **Gabriela Borin Barin:** Data curation, Formal analysis, Methodology, Writing – review & editing. **Yejin Hong:** Data curation, Formal analysis. **Juan Pablo Llinas:** Data curation, Formal analysis. **Akimitsu Narita:** Data curation, Formal analysis. **Hanuman Singh:** Data curation, Formal analysis. **Klaus Müllen:** Supervision. **Pascal Ruffieux:** Supervision, Writing – review & editing. **Roman Fasel:** Supervision, Writing – review & editing. **Jeffrey Bokor:** Supervision, Conceptualization, Writing – review & editing.

## Declaration of competing interest

The authors declare that they have no known competing financial interests or personal relationships that could have appeared to influence the work reported in this paper.

## Acknowledgement

This work was supported in part by the Office of Naval Research (ONR) MURI Program N00014-16-1-2921, the National Science Foundation (NSF) Center for Energy Efficient Electronics Science (E3S), and the NSF under award DMR-1839098. G.B.B, P.R. and R.F a acknowledge funding by the Swiss National Science Foundation under grant no. 200020_182015, the European Union Horizon 2020 research and innovation program under grant agreement no. 881603 (Graphene-Flagship Core 3), and the Office of Naval Research BRC Program under the grant N00014-18-1-2708. Additional support was provided by the Berkeley Emerging Technology Research (BETR) Center and Taiwan Semiconductor Manufacturing Company (TSMC). Device fabrication was mostly performed at the Marvell Nanofabrication Laboratory at the University of California, Berkeley (UCB). Raman spectroscopy characterization and part of the device fabrication were performed at the Molecular Foundry at Lawrence Berkeley National Laboratory (LBNL), supported by the Office of Science, Office of Basic Energy Sciences, of the U.S. Department of Energy (DOE) under contract no. DE-AC02-05CH11231. We would like to acknowledge fruitful discussions with Prof. P. Kim at Harvard University that motivated this work. We thank X. Hu and Prof. T.-J. K. Liu at UCB for assisting with the transport measurements, as well as D. Dai, C. Su, Prof. A. Zettl at UCB, and S. Aloni at LBNL for assisting with electron microscope characterizations. We also thank E. Chan, S. Dhuey, S. Shelton, T. Mattox, and A. Schwartzberg for laboratory and instrument access in the Molecular Foundry at LBNL.

## Appendix A. Supplementary data

Supplementary data to this article can be found online at https://doi.org/10.1016/j.carbon.2023.01.054.

## References

[1] Y. Liu, X. Duan, H.-J. Shin, S. Park, Y. Huang, X. Duan, Promises and prospects of two-dimensional transistors, Nature 591 (7848) (2021) 43–53.
[2] D. Akinwande, C. Huyghebaert, C.-H. Wang, M.I. Serna, S. Goossens, L.-J. Li, H.-S. P. Wong, F.H. Koppens, Graphene and two-dimensional materials for silicon technology, Nature 573 (7775) (2019) 507–518.
[3] A.C. Ferrari, F. Bonaccorso, V. Fal'Ko, K.S. Novoselov, S. Roche, P. Bøggild, S. Borini, F.H. Koppens, V. Palermo, N. Pugno, J.A. Garrido, R. Sordan, A. Bianco,

L. Ballerini, M. Prato, E. Lidorikis, J. Kivioja, C. Marinelli, T. Ryhänen, A. Morpurgo, J.N. Coleman, V. Nicolosi, L. Colombo, A. Fert, M. Garcia-Hernandez, A. Bachtold, G.F. Schneider, F. Guinea, C. Dekker, M. Barbone, Z. Sun, C. Galiotis, A.N. Grigorenko, G. Konstantatos, A. Kis, M. Katsnelson, L. Vandersypen, A. Loiseau, V. Morandi, D. Neumaier, E. Treossi, V. Pellegrini, M. Polini, A. Tredicucci, G.M. Williams, B. Hee Hong, J.-H. Ahn, J.-M. Kim, H. Zirath, B.J. van Wees, H. van der Zant, L. Occhipinti, A. Di Matteo, I.A. Kinloch, T. Seyller, E. Quesnel, X. Feng, K. Teo, N. Rupesinghe, P. Hakonen, S.R.T. Neil, Q. Tannock, T. Löfwander, J. Kinaret, Science and technology roadmap for graphene, related two-dimensional crystals, and hybrid systems, Nanoscale 7 (11) (2015) 4598–4810.

[4] J. Cai, P. Ruffieux, R. Jaafar, M. Bieri, T. Braun, S. Blankenburg, M. Muoth, A. P. Seitsonen, M. Saleh, X. Feng, K. Müllen, R. Fasel, Atomically precise bottom-up fabrication of graphene nanoribbons, Nature 466 (7305) (2010) 470–473.

[5] J. Cai, C.A. Pignedoli, L. Talirz, P. Ruffieux, H. Söde, L. Liang, V. Meunier, R. Berger, R. Li, X. Feng, K. Müllen, R. Fasel, Graphene nanoribbon heterojunctions, Nat. Nanotechnol. 9 (11) (2014) 896.

[6] G.D. Nguyen, H.-Z. Tsai, A.A. Omrani, T. Marangoni, M. Wu, D.J. Rizzo, G. F. Rodgers, R.R. Cloke, R.A. Durr, Y. Sakai, F. Liou, A.S. Aikawa, J.R. Chelikowsky, S.G. Louie, F.R. Fischer, M.F. Crommie, Atomically precise graphene nanoribbon heterojunctions from a single molecular precursor, Nat. Nanotechnol. 12 (11) (2017) 1077.

[7] L. Chen, Y. Hernandez, X. Feng, K. Müllen, From nanographene and graphene nanoribbons to graphene sheets: chemical synthesis, Angew. Chem. Int. Ed. 51 (31) (2012) 7640–7654.

[8] X. Li, X. Wang, L. Zhang, S. Lee, H. Dai, Chemically derived, ultrasmooth graphene nanoribbon semiconductors, Science 319 (5867) (2008) 1229–1232.

[9] T.H. Vo, M. Shekhirev, D.A. Kunkel, M.D. Morton, E. Berglund, L. Kong, P. M. Wilson, P.A. Dowben, A. Enders, A. Sinitskii, Large-scale solution synthesis of narrow graphene nanoribbons, Nat. Commun. 5 (1) (2014) 3189.

[10] S.R. Peurifoy, Q. Xu, R. May, N.A. Gadjieva, T.J. Sisto, Z. Jin, L.E. Marbella, C. Nuckolls, Air-stable, long-length, solution-based graphene nanoribbons, Chem. Sci. 11 (36) (2020) 9978–9982.

[11] L. Yang, C.-H. Park, Y.-W. Son, M.L. Cohen, S.G. Louie, Quasiparticle energies and band gaps in graphene nanoribbons, Phys. Rev. Lett. 99 (18) (2007), 186801.

[12] D.J. Rizzo, G. Veber, T. Cao, C. Bronner, T. Chen, F. Zhao, H. Rodriguez, S.G. Louie, M.F. Crommie, F.R. Fischer, Topological band engineering of graphene nanoribbons, Nature 560 (7717) (2018) 204–208.

[13] O. Gröning, S. Wang, X. Yao, C.A. Pignedoli, G.B. Barin, C. Daniels, A. Cupo, V. Meunier, X. Feng, A. Narita, K. Müllen, P. Ruffieux, R. Fasel, Engineering of robust topological quantum phases in graphene nanoribbons, Nature 560 (7717) (2018) 209–213.

[14] D.J. Rizzo, G. Veber, J. Jiang, R. McCurdy, T. Cao, C. Bronner, T. Chen, S.G. Louie, F.R. Fischer, M.F. Crommie, Inducing metallicity in graphene nanoribbons via zero-mode superlattices, Science 369 (6511) (2020) 1597–1603.

[15] T. Cao, F. Zhao, S.G. Louie, Topological phases in graphene nanoribbons: junction states, spin centers, and quantum spin chains, Phys. Rev. Lett. 119 (7) (2017), 076401.

[16] Q. Sun, X. Yao, O. Gröning, K. Eimre, C.A. Pignedoli, K. Müllen, A. Narita, R. Fasel, P. Ruffieux, Coupled spin states in armchair graphene nanoribbons with asymmetric zigzag edge extensions, Nano Lett. 20 (9) (2020) 6429–6436.

[17] S.K. Vadlamani, S. Agarwal, D.T. Limmer, S.G. Louie, F.R. Fischer, E. Yablonovitch, Tunnel-fet switching is governed by non-lorentzian spectral line shape, Proc. IEEE 108 (8) (2019) 1235–1244.

[18] S. Smith, J.-P. Llinás, J. Bokor, S. Salahuddin, Negative differential resistance and steep switching in chevron graphene nanoribbon field-effect transistors, IEEE Electron. Device Lett. 39 (1) (2017) 143–146.

[19] M. El Abbassi, M.L. Perrin, G.B. Barin, S. Sangtarash, J. Overbeck, O. Braun, C. J. Lambert, Q. Sun, T. Prechtl, A. Narita, K. Müllen, P. Ruffieux, H. Sadeghi, R. Fasel, M. Calame, Controlled quantum dot formation in atomically engineered graphene nanoribbon field-effect transistors, ACS Nano 14 (5) (2020) 5754–5762.

[20] S. Wang, N. Kharche, E. Costa Girão, X. Feng, K. Müllen, V. Meunier, R. Fasel, P. Ruffieux, Quantum dots in graphene nanoribbons, Nano Lett. 17 (7) (2017) 4277–4283.

[21] P.B. Bennett, Z. Pedramrazi, A. Madani, Y.-C. Chen, D.G. de Oteyza, C. Chen, F. R. Fischer, M.F. Crommie, J. Bokor, Bottom-up graphene nanoribbon field-effect transistors, Appl. Phys. Lett. 103 (25) (2013), 253114.

[22] J.P. Llinas, A. Fairbrother, G.B. Barin, W. Shi, K. Lee, S. Wu, B.Y. Choi, R. Braganza, J. Lear, N. Kau, W. Choi, C. Chen, Z. Pedramrazi, T. Dumslaff, A. Narita, X. Feng, K. Müllen, F. Fischer, A. Zettl, P. Ruffieux, E. Yablonovitch, M. Crommie, R. Fasel, J. Bokor, Short-channel field-effect transistors with 9-atom and 13-atom wide graphene nanoribbons, Nat. Commun. 8 (1) (2017) 1–6.

[23] Z. Mutlu, Y. Lin, G.B. Barin, Z. Zhang, G. Pitner, S. Wang, R. Darawish, M.D. Giovannantonio, H. Wang, J. Cai, M. Passlack, C.H. Diaz, A. Narita, K. Müllen, F.R. Fischer, P. Bandaru, A.C. Kummel, P. Ruffieux, R. Fasel, J. Bokor, Short-Channel double-gate FETs with atomically precise graphene nanoribbons, in: IEEE (Ed.) 2021 IEEE International Electron Devices Meeting (IEDM) 2021, pp. 37.4.1-37.4.4.

[24] V. Saraswat, R.M. Jacobberger, M.S. Arnold, Materials science challenges to graphene nanoribbon electronics, ACS Nano 15 (3) (2021) 3674–3708.

[25] Z. Mutlu, J.P. Llinas, P.H. Jacobse, I. Piskun, R. Blackwell, M.F. Crommie, F. R. Fischer, J. Bokor, Transfer-free synthesis of atomically precise graphene nanoribbons on insulating substrates, ACS Nano 15 (2) (2021) 2635–2642.

[26] G. Borin Barin, A. Fairbrother, L. Rotach, M. Bayle, M. Paillet, L. Liang, V. Meunier, R. Hauert, T. Dumslaff, A. Narita, K. Müllen, H. Sahabudeen, R. Berger, X. Feng, R. Fasel, P. Ruffieux, Surface-synthesized graphene nanoribbons for room temperature switching devices: substrate transfer and ex situ characterization, ACS Appl. Nano Mater. 2 (4) (2019) 2184–2192.

[27] M. Di Giovannantonio, O. Deniz, J.I. Urgel, R. Widmer, T. Dienel, S. Stolz, C. Sánchez-Sánchez, M. Muntwiler, T. Dumslaff, R. Berger, A. Narita, X. Feng, K. Müllen, P. Ruffieux, R. Fasel, On-surface growth dynamics of graphene nanoribbons: the role of halogen functionalization, ACS Nano 12 (1) (2018) 74–81.

[28] A. Berdonces-Layunta, J. Lawrence, S. Edalatmanesh, J. Castro-Esteban, T. Wang, M.S. Mohammed, L. Colazzo, D. Peña, P. Jelínek, D.G. de Oteyza, Chemical stability of (3, 1)-chiral graphene nanoribbons, ACS Nano 15 (3) (2021) 5610–5617.

[29] C. Ma, Z. Xiao, A.A. Puretzky, A.P. Baddorf, W. Lu, K. Hong, J. Bernholc, A.-P. Li, Oxidization stability of atomically precise graphene nanoribbons, Phys. Rev. Mater. 2 (1) (2018), 014006.

[30] R. Landauer, Spatial variation of currents and fields due to localized scatterers in metallic conduction, IBM J. Res. Dev. 1 (3) (1957) 223–231.

[31] M. Najari, S. Fregonese, C. Maneux, H. Mnif, N. Masmoudi, T. Zimmer, Schottky barrier carbon nanotube transistor: compact modeling, scaling study, and circuit design applications, IEEE Trans. Electron. Dev. 58 (1) (2010) 195–205.

[32] P. Michetti, G. Iannaccone, Analytical model of one-dimensional carbon-based Schottky-barrier transistors, IEEE Trans. Electron. Dev. 57 (7) (2010) 1616–1625.

[33] P.M. Solomon, Contact resistance to a one-dimensional quasi-ballistic nanotube/wire, IEEE Electron. Device Lett. 32 (3) (2011) 246–248.

[34] G. Pitner, G. Hills, J.P. Llinas, K.-M. Persson, R. Park, J. Bokor, S. Mitra, H.-S. P. Wong, Low-temperature side contact to carbon nanotube transistors: resistance distributions down to 10 nm contact length, Nano Lett. 19 (2) (2019) 1083–1089.

[35] I.A. Verzhbitskiy, M.D. Corato, A. Ruini, E. Molinari, A. Narita, Y. Hu, M. G. Schwab, M. Bruna, D. Yoon, S. Milana, Raman fingerprints of atomically precise graphene nanoribbons, Nano Lett. 16 (6) (2016) 3442–3447.

[36] M. Vandescuren, P. Hermet, V. Meunier, L. Henrard, P. Lambin, Theoretical study of the vibrational edge modes in graphene nanoribbons, Phys. Rev. B 78 (19) (2008), 195401.

[37] Z. Chen, W. Zhang, C.-A. Palma, A. Lodi Rizzini, B. Liu, A. Abbas, N. Richter, L. Martini, X.-Y. Wang, N. Cavani, Synthesis of graphene nanoribbons by ambient-pressure chemical vapor deposition and device integration, J. Am. Chem. Soc. 138 (47) (2016) 15488–15496.

[38] L. Martini, Z. Chen, N. Mishra, G.B. Barin, P. Fantuzzi, P. Ruffieux, R. Fasel, X. Feng, A. Narita, C. Coletti, Structure-dependent electrical properties of graphene nanoribbon devices with graphene electrodes, Carbon 146 (2019) 36–43.

[39] V. Passi, A. Gahoi, B.V. Senkovskiy, D. Haberer, F.R. Fischer, A. Grüneis, M. C. Lemme, Field-effect transistors based on networks of highly aligned, chemically synthesized N= 7 armchair graphene nanoribbons, ACS Appl. Mater. Interfaces 10 (12) (2018) 9900–9903.

[40] A. Ishii, A. Shiotari, Y. Sugimoto, Quality control of on-surface-synthesised seven-atom wide armchair graphene nanoribbons, Nanoscale 12 (12) (2020) 6651–6657.

[41] A. Fairbrother, J.-R. Sanchez-Valencia, B. Lauber, I. Shorubalko, P. Ruffieux, T. Hintermann, R. Fasel, High vacuum synthesis and ambient stability of bottom-up graphene nanoribbons, Nanoscale 9 (8) (2017) 2785–2792.

[42] A.D. Franklin, Z. Chen, Length scaling of carbon nanotube transistors, Nat. Nanotechnol. 5 (12) (2010) 858–862.

[43] M. Pizzochero, K. Čerņevičs, G.B. Barin, S. Wang, P. Ruffieux, R. Fasel, O. V. Yazyev, Quantum electronic transport across 'bite'defects in graphene nanoribbons, 2D Mater. 8 (3) (2021), 035025.

[44] C.-S. Lee, E. Pop, A.D. Franklin, W. Haensch, H.-S. Wong, A compact virtual-source model for carbon nanotube FETs in the sub-10-nm regime—Part I: intrinsic elements, IEEE Trans. Electron. Dev. 62 (9) (2015) 3061–3069.

[45] R.M. Jacobberger, E.A. Murray, M. Fortin-Deschênes, F. Göltl, W.A. Behn, Z. J. Krebs, P.L. Levesque, D.E. Savage, C. Smoot, M.G. Lagally, Alignment of semiconducting graphene nanoribbons on vicinal Ge (001), Nanoscale 11 (11) (2019) 4864–4875.

[46] M. Luisier, M. Lundstrom, D.A. Antoniadis, J. Bokor, Ultimate Device Scaling: Intrinsic Performance Comparisons of Carbon-Based, InGaAs, and Si Field-Effect Transistors for 5 Nm Gate Length, 2011 International Electron Devices Meeting, IEEE, 2011, 11.2. 1-11.2. 4.

[47] G. Pitner, Z. Zhang, Q. Lin, S.-K. Su, C. Gilardi, C. Kuo, H. Kashyap, T. Weiss, Z. Yu, T.-A. Chao, Sub-0.5 nm interfacial dielectric enables superior electrostatics: 65 mV/dec top-gated carbon nanotube FETs at 15 nm gate length, in: 2020 IEEE International Electron Devices Meeting (IEDM), IEEE, 2020, pp. 3.5. 1–3.5. 4.